Check for updates

ADVANCED PHYSICS RESEARCH Open Access

www.advphysicsres.com

Deeper Insight into the Mechanisms Behind Sputter Damage in Silicon Solar Cells Based on the Example of Nanocrystalline Silicon Carbide

Alexander Eberst, Binbin Xu, Karsten Bittkau, Weiyuan Duan, Andreas Lambertz, Ansgar Meise, Marc Heggen, Rafal E. Dunin-Borkowski, Uwe Rau, and Kaining Ding*

Transparent conducting oxides, like indium tin oxide, enable lateral charge carrier transport in silicon heterojunction solar cells. However, their deposition can damage the passivation quality in the solar cell. This damage during the sputter deposition is a complex issue that has not been fully understood, particularly in various silicon-based materials like amorphous silicon, polycrystalline silicon, or nanocrystalline silicon carbide. The degradation in passivation quality observed in, for example, amorphous silicon is not only explainable by UV light degradation. This study explores the origin of this degradation based on the example of hydrogenated nanocrystalline silicon carbide by combining simulations with experimental analyses. It delves into potential sources of damage during the sputtering process and determines that neither primary nor secondary effects from plasma luminescence or electron bombardment are likely contributors to the damage. Similarly, the implantation of ions, as well as the creation of vacancies and ionization of lattice atoms, are also considered improbable causes. It is, however, proposed that the transfer of energy to the crystalline silicon interface via phonons can factor into the degradation of the passivation quality. This transfer might be a plausible explanation for the damage observed in the passivation layers during the sputtering process.

1. Introduction

State-of-the-art silicon heterojunction (SHJ) or transparent passivating contact (TPC) solar cells enable high device voltages due to the excellent passivation quality of the applied hydrogenated amorphous silicon (a-Si:H) or hydrogenated nanocrystalline silicon carbide (nc-SiC:H) layers, respectively. In both structures, the use of a transparent conductive oxide (TCO) is often necessary due to the low conductivity of the thin layers applied. TCOs, such as sputtered indium tin oxide (ITO), are therefore critical to improve the lateral charge carrier transport in the solar cell structure.[1] However, the sputtering process to apply TCOs exposes the underlying layers, such as a-Si:H or nc-SiC:H, to various influences. These influences can detrimentally affect the passivation quality of these layers, leading to a degraded performance of the solar cells. This issue, known as ‘sputter damage’, presents challenges in multiple solar cell structures, including a-Si:H-based SHJ solar cells, polycrystalline silicon (poly-Si)-based solar cells, and nc-SiC:H-based TPC solar cells.[2–6]

The origin of sputter damage remains unclear due to the multitude of potential factors during the sputtering process. For instance, due to the argon and oxygen plasma, UV radiation is present. This is known to damage the passivation quality from, for example, a-Si:H, but it cannot fully explain the extent of the damage observed.[5,7] Similarly, in polycrystalline silicon-based approaches, UV degradation is not evident,[6] while the passivation quality of nc-SiC:H is known to degrade when exposed to pure O_2 plasma.[2] The further identification of sources for both recoverable and non-recoverable damage remains an ongoing research area.

This study aims to combine simulations with experimental approaches to identify potential origins of sputter damage in silicon-based materials. It proposes a hypothesis regarding the unclear source of passivation quality degradation, focusing on hydrogenated nanocrystalline silicon carbide-based transparent passivating contact solar cells.

A. Eberst, B. Xu, K. Bittkau, W. Duan, A. Lambertz, U. Rau, K. Ding
IEK-5 Photovoltaik
Forschungszentrum Jülich GmbH
DE-52428 Jülich, Germany
E-mail: a.eberst@fz-juelich.de

A. Eberst, B. Xu, U. Rau
Jülich Aachen Research Alliance (JARA-Energy) and Faculty of Electrical Engineering and Information Technology
RWTH Aachen University
Schinkelstr. 2, 52062 Aachen, Germany

A. Meise, M. Heggen, R. E. Dunin-Borkowski
Ernst Ruska-Centre for Microscopy and Spectroscopy with Electrons (ER-C)
Forschungszentrum Jülich GmbH
DE-52428 Jülich, Germany

The ORCID identification number(s) for the author(s) of this article can be found under https://doi.org/10.1002/apxr.202400036

© 2024 The Author(s). Advanced Physics Research published by Wiley-VCH GmbH. This is an open access article under the terms of the Creative Commons Attribution License, which permits use, distribution and reproduction in any medium, provided the original work is properly cited.

DOI: 10.1002/apxr.202400036

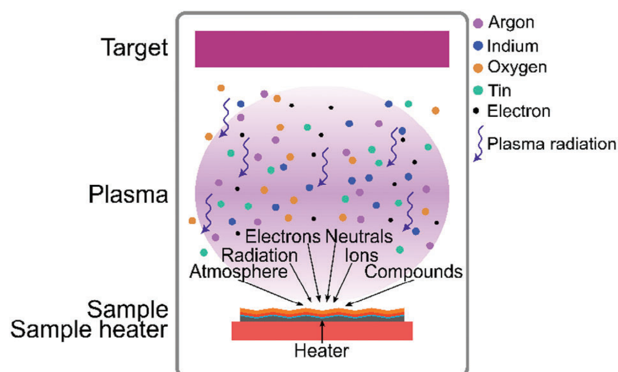

Figure 1. Overview of different influences on the sample during the sputtering process. The four main factors are influences from process-related parameters, electrons, light emitted from the plasma, and ions, neutrals, and compounds.

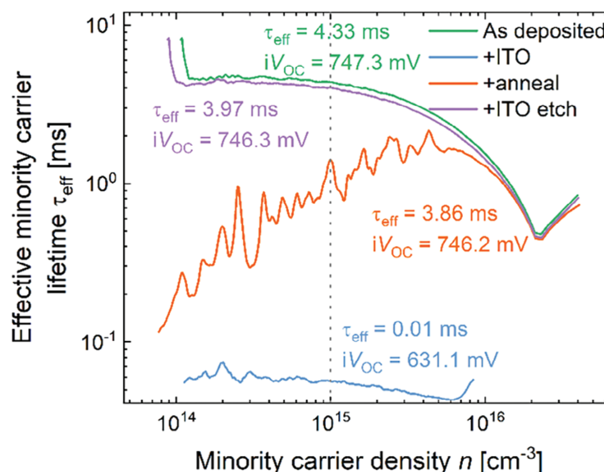

Figure 2. Measured effective lifetime curves for samples symmetrically passivated with the TPC structure. Lifetime curves for the as-deposited state, as well as after the ITO deposition, after an annealing step, and with the ITO etched away are presented. The as-deposited and ITO etched curves are nearly identical. The dashed line indicates the minority charge carrier concentration of $n = 10^{15}$ cm^{-3}, at which the effective lifetime is determined.

2. Background of Sputter Damage

Figure 1 shows an overview of some of the various species and influences on the sample involved in the sputtering process. The influences can be grouped into four categories, including effects from the process environment itself, as well as electrons, light, and ions or particles emitted from the plasma or the sputter target.

During sputtering, the sample is heated, which may lead to material degradation if excessive heating occurs. This is coupled with exposure to the sputtering atmosphere, containing sputter or doping gases such as argon (Ar) and oxygen (O), which can further impact the properties of the material. Electrons escaping from the plasma directly impact the sample and may induce secondary electrons and X-rays within the films. Such interactions may also damage the sample.

Another significant factor is the light emitted by the plasma. For example, the emission peak from the oxygen plasma at 9.5 eV, and even higher energies for the argon plasma,[7] possess enough energy to potentially break silicon-hydrogen bonds with binding energies between 3.55 and 3.92 eV,[8–10] or the strong silicon-silicon bonds with binding energies of ≈2.5 eV.[11]

Furthermore, ions, neutrals, and compounds present during the sputtering process might also play a crucial role. These particles, whether accelerated toward the sample or neutralized and then reflected toward the sample,[12,13] can be implanted in the film. Implanted particles bring in additional energy to the sample and can penetrate the crystalline silicon interface, disturbing the lattice and creating defects either along their path or at the implantation sites. The energy transfer from the ions during the braking process could further ionize layer atoms or create phonons and vacancies. In amorphous silicon, Illiberi et al. proposed that the impinging ions create a bound electron–hole pair, known as an exciton. This exciton moves toward the crystalline silicon interface, recombines non-radiatively, breaks the silicon (Si)-hydrogen (H) bond through the released energy, and displaces the H necessary for passivation.[5] Moreover, phonons can have energies according to their dispersion relation,[14] which they release when they dissipate, for example, due to lattice defects at the crystalline silicon interface. The released energy of multiple phonons could displace the hydrogen necessary for chemical passivation, while the created vacancies could strain the lattice, influencing passivation.

Sputter damage is typically categorized based on its recoverability. Non-recoverable damage includes the creation of additional defects at the interface[15] that may not be passivated due to ion implantation, or the loss of hydrogen[16] required for passivation due to excessive heating of the sample during the sputtering process, losing it for the purpose of passivation. On the other hand, recoverable damage could result from the displacement of atoms and the breaking of bonds essential for passivation, like hydrogen or silicon.[4] As the hydrogen remains in the sample, it is available for re-passivation of the created dangling bonds. Subsequent annealing or light soaking treatments allow displaced atoms to regain enough energy to return to their original location and reform the bond, re-passivating the previously created defect.[4,5]

3. Influence of the Sputtering Process on the Material Properties

In silicon carbide-based TPC structures, an initial degradation in passivation quality, particularly in terms of implied open-circuit voltage (iV_{OC}), is observed. However, this sputter damage is almost entirely reversible through a low-temperature annealing step at 230 °C for 20 min, as indicated in **Figure 2**. The remaining damage of ≈3 mV might be due to a distortion of the effective lifetime curve at low injection levels caused by the ITO layer.[17] After the ITO is removed, the effective lifetime curve is nearly identical to the as-deposited curve. This strong initial degradation could either imply a microstructural change in the material or an alteration in the hydrogen configuration.

To investigate these possibilities, Fourier-transform infrared (FTIR) and Raman spectroscopy were employed. **Figure 3**a,b

© 2024 The Author(s). Advanced Physics Research published by Wiley-VCH GmbH
27511200, 2024, 9, Downloaded from https://onlinelibrary.wiley.com/doi/10.1002/apxr.202400036, Wiley Online Library on [11/09/2024]. See the Terms and Conditions (https://onlinelibrary.wiley.com/terms-and-conditions) on Wiley Online Library for rules of use; OA articles are governed by the applicable Creative Commons License

27511200, 2024, 9, Downloaded from https://onlinelibrary.wiley.com/doi/10.1002/apxr.202400036, Wiley Online Library on [11/09/2024]. See the Terms and Conditions (https://onlinelibrary.wiley.com/terms-and-conditions) on Wiley Online Library for rules of use; OA articles are governed by the applicable Creative Commons License

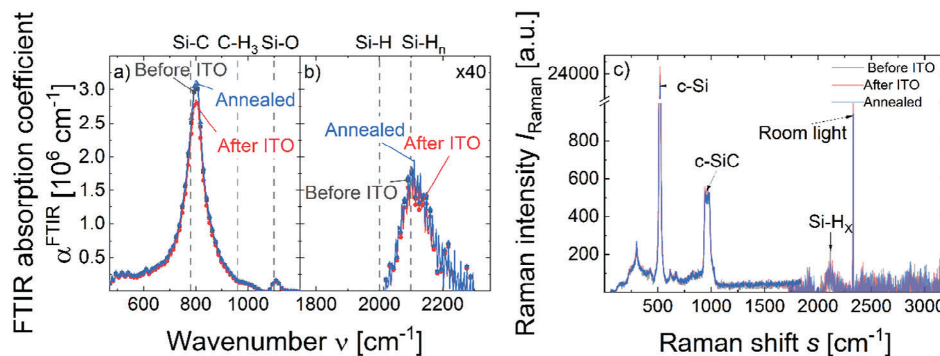

Figure 3. FTIR and Raman measurements before and after ITO deposition and subsequent annealing. No change in the measured microstructure is visible.

display the FTIR spectra for the Si- carbon (C and Si-H$_n$ bonding regimes, respectively, while Figure 3c presents the Raman spectra of the sample at different processing stages: before ITO deposition, after ITO deposition, and post-annealing. Before the post-ITO-deposition measurements, the ITO is removed by a dip in hydrochloric acid to enable an undisturbed measurement. Notably, no discernible differences are observed between these three states in either characterization technique. Moreover, when the ITO layer is removed by etching, electrical conductivity measurements, as shown in Table S1 (Supporting Information), show no variation before and after ITO deposition or subsequent annealing in any processing combination. Since the conductivity is largely dependent on grain sizes, which correlate with the intensity of the FTIR Si-C peak,[18] no overall microstructural changes are found.

On the other hand, the iV_{OC} is primarily influenced by the hydrogen content, which is expected to be visible in variations in the Si-H$_n$ peak intensities. The absence of any detectable change across the three processing stages suggests that transmission FTIR might not be sensitive enough to detect the changes at the crystalline silicon interface as the passivation quality is severely degraded. Furthermore, the impact of sputter damage might be masked by the strong Si-H$_n$ signal from the nc-SiC:H bulk. For a-Si:H, a more sensitive approach using attenuated total reflection-FTIR revealed changes in the Si-H$_n$ FTIR signal. As highlighted by Demaurex et al.,[4] particularly the high stretching mode is reduced following ITO sputtering. While annealing restores passivation, it fails to revert the Si-H configuration to its original state, resulting in a permanent deformation of the Si–H mode compared to its initial condition.[4]

4. Influences of the Process Conditions, Light and Electrons

Figure 4 presents the iV_{OC} for different variations of the reference sputter process, including scenarios where only the process gases are introduced without plasma ignition, and with the sample heater deactivated, both before and after ITO deposition and annealing. The usual degradation is observed in the reference process. The process without plasma ignition does not cause any degradation, indicating that the gas atmosphere itself does not damage the passivation quality of the sample. On the other hand, deactivation of the sample heater leads to an increase in damage compared to the reference process. However, in all cases, the damage is reversible through the subsequent annealing step. This observation suggests that, while the gas atmosphere is not harmful, the heater temperature is a critical parameter to control the initial damage. The increase in damage when the heater is off could imply an in situ annealing effect from the heater, though an alternative explanation is considered later in the study.

To distinguish between the effects of plasma-emitted light and the impacts of electrons and ions on the sample, the sample is shielded using various filter glasses that block different wavelength ranges of plasma emission. **Figure 5a,b** display photoluminescence lifetime (PL) images post-ITO deposition and post-annealing, respectively. Figure 5c shows the emissions from argon and oxygen plasma along with the transmission through the different filter glasses applied. Filter A partially blocks the highest-energy vacuum UV (VUV) light from the plasma, while filter B blocks a broader part of the UV spectrum. Filter C allows only the transmission of light with an energy below the UV-A regime, and filter D effectively blocks all plasma-emitted light.

Despite previous findings that oxygen plasma can degrade the passivation quality of nc-SiC:H based contacts,[2] no such degradation was observed in this study under any filter glass, even those transmitting VUV light. The initial nanometers of the deposited ITO might already sufficiently shield the sample, and any exposure to plasma luminescence before the shielding effect of the ITO film might be too short or with a too low intensity to cause any degradation. The recoverability of the sputtering damage is again highlighted in Figure 5b, where the undamaged areas covered by filter glass are nearly undetectable in the PL image post-annealing, save for some residual degraded shades possibly resulting from sample handling. Consequently, light emitted from the plasma is ruled out as a source of damage, leaving electrons and ions as the remaining possible sources of degradation.

The investigation of the effect of electrons on sputter damage includes both simulations and experimental approaches. In the simulations, variables such as the hydrogen concentration (c_H) in the material, the incident energy of the electrons ($E_{in}^{electron}$), and the crystallinity (X_C) of the material is varied. As an example, **Figure 6a** illustrates the normalized intensity (I^{norm}) against the sample depth (d) for various $E_{in}^{electron}$ values. The simulations reveal that even at an elevated incident energy up to 500 eV, the electron penetration depth remains within the first 10 nanometers. The penetration depth is affected by the crystallinity of the

© 2024 The Author(s). Advanced Physics Research published by Wiley-VCH GmbH

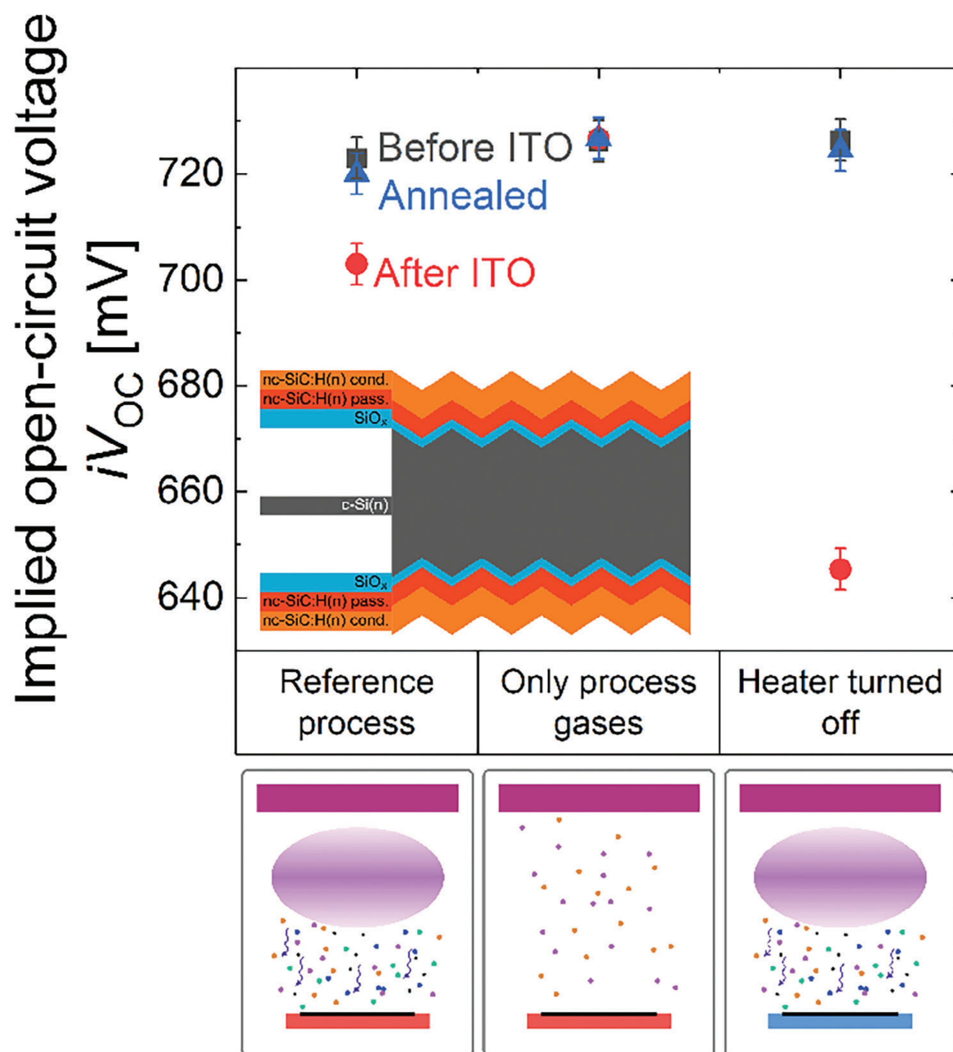

Figure 4. Effects of the process gases and the heater temperature compared to the reference process on the implied open-circuit voltage. While the process atmosphere has no impact, the reduced heater temperature significantly increases the sputter damage.

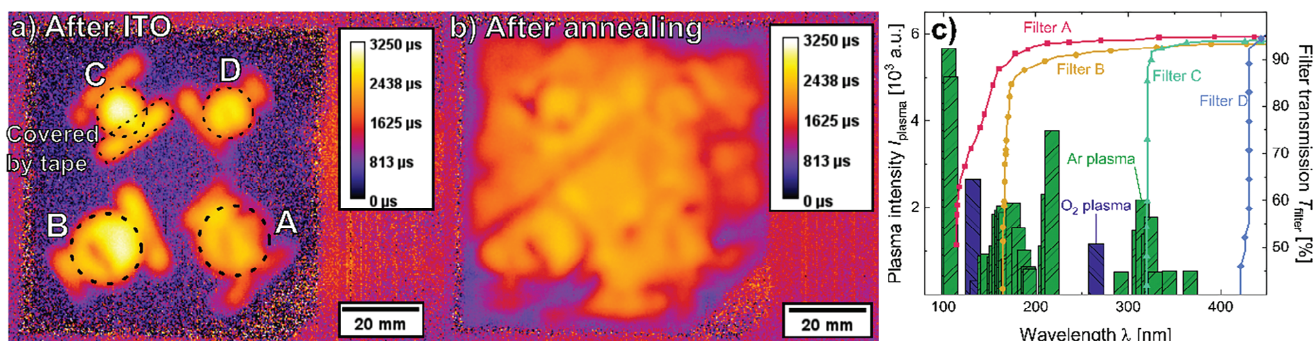

Figure 5. A sample shielded with various filter glasses a) after ITO deposition and b) after subsequent annealing. No degradation in the shielded area is visible and the surrounding damage is completely restorable. c) Light spectrum emitted from the plasma extracted from[7] and transmission spectra of the filter glasses as given by the manufacturers.

© 2024 The Author(s). Advanced Physics Research published by Wiley-VCH GmbH

27511200, 2024, 9, Downloaded from https://onlinelibrary.wiley.com/doi/10.1002/apxr.202400036, Wiley Online Library on [11/09/2024]. See the Terms and Conditions (https://onlinelibrary.wiley.com/terms-and-conditions) on Wiley Online Library for rules of use; OA articles are governed by the applicable Creative Commons License

27511200, 2024, 9, Downloaded from https://onlinelibrary.wiley.com/doi/10.1002/apxr.202400036, Wiley Online Library on [11/09/2024]. See the Terms and Conditions (https://onlinelibrary.wiley.com/terms-and-conditions) on Wiley Online Library for rules of use; OA articles are governed by the applicable Creative Commons License

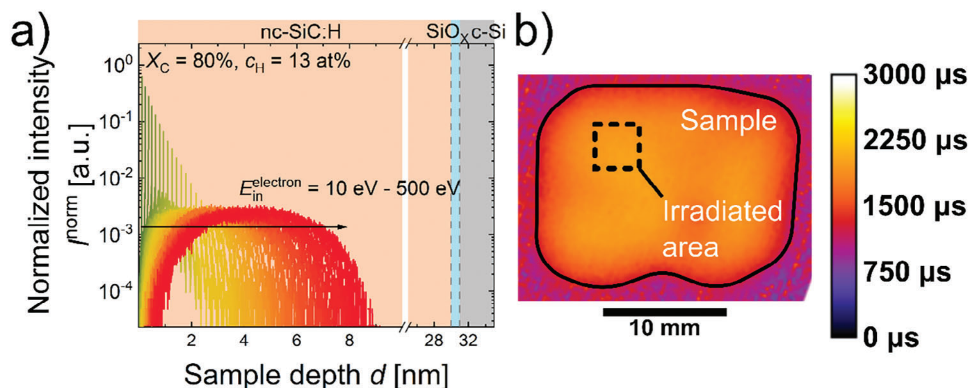

Figure 6. a) Simulated electron penetration depth into the layer for energies between 10 and 500 eV. The penetration depth for the estimated process conditions is 3.9 nm. b) Photoluminescent lifetime image after scanning an area with a 500 eV electron beam. No degradation is visible in the scanned area.

material, as shown in Figure S1a (Supporting Information). It ranges from 3.7 nm for $X_C = 0\%$, which accounts for amorphous channels between vertically growing grains,[19] to 5 nm for $X_C = 100\%$ within the grains. Figure S1b (Supporting Information) indicates that the hydrogen content has a minimal impact, with a consistent penetration depth ≈4 nm. Under assumed material and process conditions with a X_C of 80%, c_H of 13 at%, and an $E_{in}^{electron}$ of 270 eV, the maximum simulated penetration depth for electrons is 3.9 nm. Given that the layer stack thickness exceeds 20 nm, the direct impact of electrons on the passivation quality of the sample appears to be negligible.

Furthermore, the primary electron can potentially generate secondary electrons and, in this process, X-ray radiation, as well as braking radiation from the deceleration of primary electrons, is considered. The carbon K_α line, with an energy of 277 eV, is the lowest X-ray line among the involved elements.[20] Therefore, it is expected that no secondary electrons and X-ray radiation from secondary electron generation are emitted, as the incident energy in the employed process is lower. Simulations varying the incident energy in Figure S2 (Supporting Information) show that X-ray generation begins only at $E_{in}^{electron}$ of 290 eV and occurs within the first few angstroms of the layer. The results of the simulations indicate that the electron bombardment does not affect the crystalline silicon interface and does not damage the passivation quality of the crystalline silicon.

To underline the simulation results, an experimental verification is conducted. A section of a symmetrically passivated TPC sample is scanned using a scanning electron microscope with an acceleration voltage of 500 V, as indicated in the PL image in Figure 6b. The irradiated area shows no signs of degradation, confirming the simulation predictions that direct electron impact and secondary effects like X-ray and secondary electron generation are not the sources of sputter damage, as they should be present at these high $E_{in}^{electron}$. This finding also rules out braking radiation from electron deceleration in the material as a damaging factor.

5. Influence of Ions and their Secondary Effects

During the sputtering process, ions can be implanted in the underlying layer or lead to secondary effects such as the formation of vacancies, ionization of atoms, or generating phonons. This ion implantation can disrupt the lattice structure of the layer and produce defects. Simulations can model the ion impingement process. **Figure 7a–d** displays the ion distribution for the single-charged elements involved in the sputtering process: oxygen, argon, indium (In), and tin (Sn), under varying X_C. Among these, oxygen ions penetrate the deepest due to their smaller size, while argon, indium, and tin all have similar penetration depths, which increase for a decreasing X_C. Even in amorphous layers, the maximum simulated penetration depth is only 5.9 nm for the oxygen ions. The hydrogen concentration within the material does not influence this penetration depth, as illustrated in Figure S4 (Supporting Information). With incident energies of oxygen ions up to 750 eV, including double-charged oxygen ions, the penetration depth only reaches 8.9 nm, as shown in Figure S3 (Supporting Information). For the material parameters assumed in the simulation, the maximum penetration depth of oxygen is simulated to be 4.5 nm, which is still at a significant distance from the crystalline silicon interface.

To validate these simulation results, an energy dispersive X-ray (EDX) line scan along the layer stack after the ITO deposition is performed. The results of which are displayed in Figure 7e. Due to the imperfect alignment of the sample, the interface of the nc-SiC:H(n) is not sharply defined but is identified at the inflection point of the slope of the measured signal. This approach suggests an approximate measured penetration depth of 3.7 nm for oxygen, indicating that the simulations slightly overestimate the actual penetration. The simulated and actual measured penetration depths are summarized in **Table 1**. For heavier ions, the measured penetration depth is even less than the simulated one, suggesting that ion implantation is a superficial process. Therefore, ion implantation as a cause for the observed degradation in the passivation quality of the layer stack can be ruled out. This leaves only the secondary effects of ion impact as potential reasons for the degradation.

When oxygen ions accelerate during the sputtering process and hit the surface layer, simulations indicate that ≈60% of their energy is transferred to phonons, ≈35% to the electrons of the sample layers, in the following named ionization, and ≈5% contributes to vacancy creation. For larger ions, the energy distribution shifts slightly, channeling ≈5% less into ionization and more

 © 2024 The Author(s). Advanced Physics Research published by Wiley-VCH GmbH

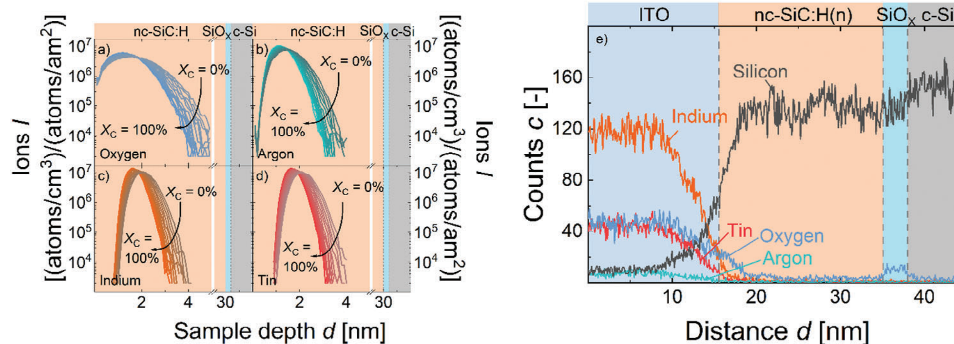

Figure 7. Simulated ion implantation depth of a) oxygen, b) argon, c) indium, and d) tin for crystallinities ranging from 0% to 100%. For the estimated material conditions, oxygen penetrates the deepest with an implantation depth of 4.8 nm. e) EDX line scan of a sample after ITO deposition. The measured deepest implantation depth is for oxygen with a depth of 3.7 nm.

Table 1. Comparison of simulated and measured implantation depth for various ions. Oxygen penetrates the deepest into the sample.

Ion	Measured Penetration [nm]	Simulated Penetration [nm]
In, Sn, Ar	≈1.7 nm	3.4 nm
O	3.7 nm	4.5 nm

into phonons, while the energy for vacancy generation remains roughly constant.

The vacancies are generated if impinging ions penetrate the layer and possess sufficient energy to displace a layer atom from its lattice site, meaning the vacancies are shallower than the maximum penetration depth of the ion. The deepest silicon vacancy is simulated at 4 nm in the layer. Vacancy movement, depicted in **Figure** 8a, can occur through nearest-neighbor or second-neighbor hopping. For carbon vacancies (V(C)) i), a silicon atom may move to the carbon site, creating an antisite (Si(C)), leaving a silicon vacancy (V(Si)), or an adjacent carbon atom may fill the vacancy. This movement mechanism is likely the most prevalent, as the silicon antisite-vacancy complex is unstable.[21] Silicon vacancies ii) can migrate directly by a neighboring silicon atom filling the vacancy or through the formation of a carbon vacancy-carbon antisite (C(Si)) complex. The carbon antisite might then move on the silicon sublattice or the carbon vacancy moves on the carbon sublattice. These migration processes have high energy barriers of several electronvolts, and the movement and annealing of both vacancy types only occur at temperatures of 500 °C for the carbon vacancy or 750 °C for the silicon vacancy.[22–26] As

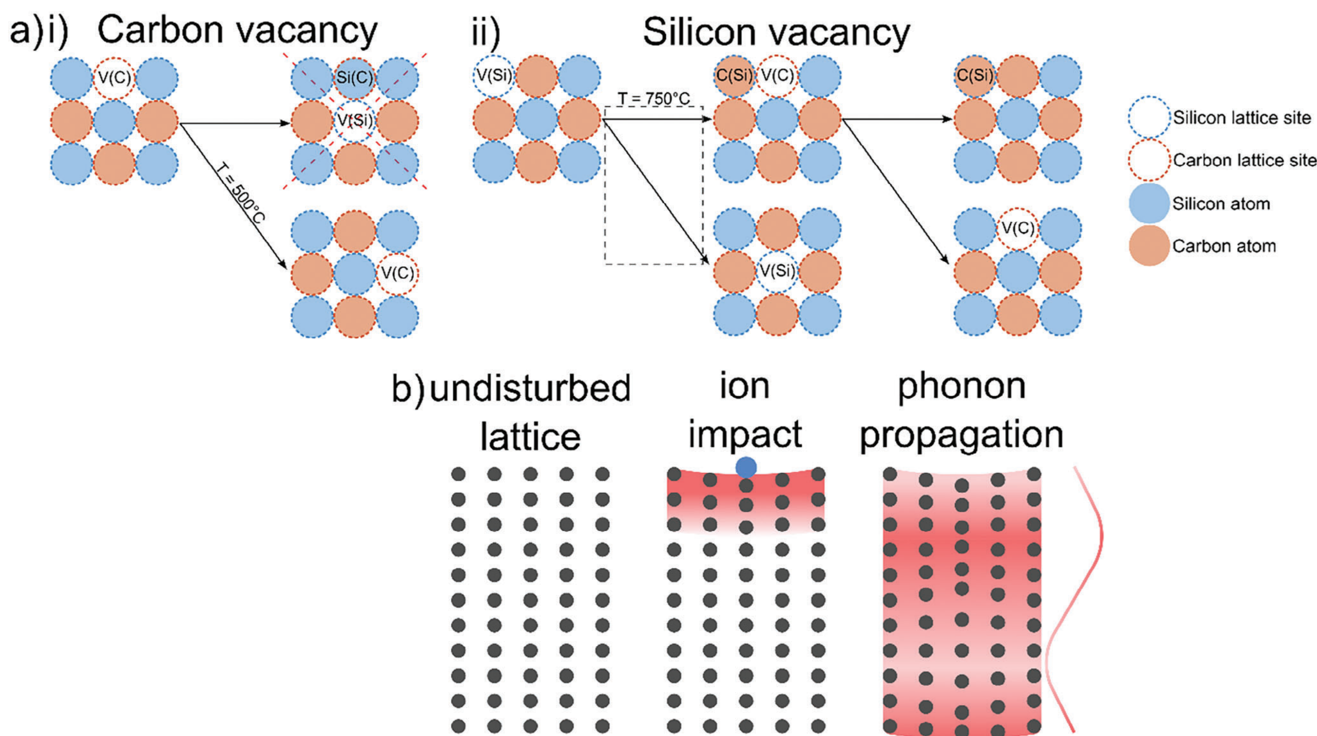

Figure 8. Overview of the secondary effects of the ion impact. a) Movement processes for i) the carbon and ii) the silicon vacancy and b) Phonon generation and propagation after the ion impact.

© 2024 The Author(s). Advanced Physics Research published by Wiley-VCH GmbH

27511200, 2024, 9, Downloaded from https://onlinelibrary.wiley.com/doi/10.1002/apxr.202400036, Wiley Online Library on [11/09/2024]. See the Terms and Conditions (https://onlinelibrary.wiley.com/terms-and-conditions) on Wiley Online Library for rules of use; OA articles are governed by the applicable Creative Commons License

low-temperature annealing of 230 °C is sufficient to completely restore the degradation of the passivation quality, vacancy migration at these annealing temperatures seems impossible. Thus, any low-temperature annealing should be insufficient to remove the vacancies and restore the degradation of the passivation quality. Therefore, vacancies are likely not the origin of the sputtering damage.

Moreover, part of the energy of the incident ion is transferred to the electrons of the bombarded layer. This might excite electrons or generate free electrons. The resulting free electrons do not impact the passivation of the sample, as previously shown through electron beam irradiation. A proposed mechanism for damage in amorphous silicon suggests that ions generate bound electron–hole pairs, called excitons, as indicated by Illiberi et al..[5] These excitons are supposed to migrate to the crystalline silicon interface and recombine non-radiatively, displacing hydrogen atoms with the released energy and thus affecting the passivation quality of the crystalline silicon. Even though, given that the diffusion length for minority charge carriers in both intrinsic and p-type amorphous silicon, as well as silicon carbide, is over 100 nm,[27,28] the movement of excitons over tens of nanometers, in the case of TPCs, in these materials seems highly improbable. Unlike minority carriers that require another charge carrier of opposite polarity for recombination, excitons consist of bound pairs of both carrier polarities. The high density of defects in doped amorphous or nanocrystalline materials provides numerous potential trap states for immediate recombination of excitons, as the electron and hole are already in close vicinity of each other. Consequently, it is plausible that the release of mobile hydrogen from non-radiatively recombining excitons is no significant factor in degrading the passivation at the crystalline silicon interface. Other direct electron-related damage mechanisms from free electrons or X-ray generation have been previously disregarded.

Another possible interaction involves the excitation of an electron by the incident ion without its ejection from the atom. This excited electron relaxes to its ground state, releasing the excess energy, possibly as UV radiation. However, due to the absence of data comparing the intensity of this UV emission with the UV radiation emitted from the plasma, it is challenging to conclude the significance of this effect.

Phonons, which are quantized lattice waves, exist in acoustic and optical modes. In the acoustic mode, typically lower in energy, lattice ions within the same unit oscillate in phase, whereas in the optical mode, generally higher in energy, they oscillate in opposite phases. In crystalline silicon carbide, the highest phonon energies are identified at 120 meV in the optical branch and 80 meV in the acoustic branch.[14] The mean-free path of phonons in crystalline materials can extend to hundreds of nanometers.[29,30] However, given that phonons require a lattice structure for propagation, their impact on amorphous materials, where sputter damage is also observed, should be minimal.

In amorphous silicon, phonon-like modes with mean-free paths exceeding 100 nm have been found,[31,32] significantly influencing heat transport within the material. Consequently, it is plausible that the energy conveyed through phonons and phonon-like modes is substantial. These phonons might transport the energy from the incident ion through layers such as nc-SiC:H. If the lattice is disrupted at the nc-SiC:H/SiO_X/c-Si interface, the phonons cannot further propagate and dissipate, releasing their energy. This process, including the initial ion impact and the phonon propagation, is schematically depicted in Figure 8b. If multiple high-energy optical phonons dissipate simultaneously, the released energy could be sufficient to break silicon-hydrogen bonds, displacing hydrogen, creating an open silicon bond, and degrading the passivation quality of the crystalline silicon. Since hydrogen remains in close proximity to the broken bond, lower temperature annealing can effectively reattach hydrogen to the open silicon bonds, re-passivating the sample and potentially reversing the damage. As this might alter the hydrogen configuration at the crystalline silicon interface, this process could account for the shift in FTIR spectra observed by Demaurex et al.[4] The energy profile proposed for this mechanism is illustrated in **Figure 9**.

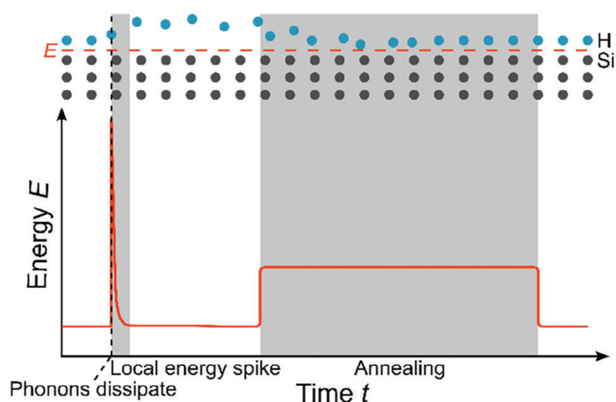

Figure 9. Expected energy profile at the crystalline silicon interface for the phonon dissipation process with subsequent annealing. The movement of hydrogen atoms is sketched at the top.

The transmission of energy to the interface via phonons aligns with earlier observations of increased damage at reduced heater temperatures in this study. Lower temperatures lead to longer mean-free paths of phonons, allowing more phonons to reach the interface and making energy spikes high enough to displace more hydrogen more probable, which increases the passivation damage. While the increased damage at lower heater temperatures could also result from in situ annealing, the temperatures required to reverse sputter damage in silicon carbide surpass those tolerable by amorphous silicon. Reduced annealing temperatures significantly prolong the repair time of the damage, up to several hours, or might not fully restore the damage at all. At higher temperatures, hydrogen effusion from the amorphous silicon on the rear side of transparent passivated contact solar cells severely degrades the passivation quality. Thus, the increased damage at lower heater temperatures is likely primarily due to the extended mean-free path of phonons, leading to more phonons reaching the crystalline silicon interface.

6. Conclusion

This study focuses on the impact of sputtering on the passivation of silicon-based materials, using hydrogenated nanocrystalline silicon carbide as an example. A comprehensive analysis is conducted, combining simulations and experiments to explore

 © 2024 The Author(s). Advanced Physics Research published by Wiley-VCH GmbH

27511200, 2024, 9, Downloaded from https://onlinelibrary.wiley.com/doi/10.1002/apxr.202400036, Wiley Online Library on [11/09/2024]. See the Terms and Conditions (https://onlinelibrary.wiley.com/terms-and-conditions) on Wiley Online Library for rules of use; OA articles are governed by the applicable Creative Commons License

both the direct and secondary effects of the various influences inflicted on the sample during the sputtering process. The findings categorize sputter damage into recoverable and non-recoverable damage. Non-recoverable damage involves direct harm to the interface, such as ion implantation creating new defects. Recoverable damage occurs when the energy from ions is transferred to the crystalline silicon interface, leading to the de-passivation of silicon bonds, which is promoted by mechanisms like breaking silicon-hydrogen bonds and displacing hydrogen atoms. However, such damage can be reversed in subsequent annealing or light soaking steps, as the displaced hydrogen can migrate back to the now-open silicon bond and re-saturate it, thus re-passivating the surface.

The study rules out the effects of the gas atmosphere present during deposition as a potential source of damage, as no passivation degradation is observed in the absence of plasma ignition. Conversely, reducing the sample heater temperature to room temperature increases the damage significantly, but it remains fully recoverable. This increased damage may be due to an extended mean-free path of phonons, which affects the passivation quality detrimentally.

Experimental evidence shows that plasma luminescence does not degrade the passivation quality, as indicated by the absence of degradation in areas shielded by filter glasses, which transmit different parts of the emitted spectrum. Furthermore, exposing the sample to a high-energy electron beam does not affect the passivation quality. Simulations underline this by showing that electrons penetrate only up to 3.9 nm into the layer, and secondary effects such as X-ray and secondary electron generation are also ruled out as causes of damage.

The ion impact is thoroughly investigated through both simulations and experiments. Present ions, particularly oxygen ions, exhibit only superficial penetration within the first 3.7 nm and induce secondary effects within this range. It is unlikely that vacancies generated by the ion impact would propagate through the sample, given the high temperatures required for such movement. Free electrons resulting from ionization are expected to behave similarly to those in the electron beam experiments and thus not contribute to degradation. Any potential UV light generated from excited electrons that relax back to their ground state, whose intensity might be higher than the one generated by the plasma, is a possibility that needs further investigation. However, phonons or phonon-like modes, with mean-free paths exceeding 100 nm, enable long-range energy transfer. The simultaneous dissipation of multiple high-energy phonons at the crystalline silicon interface could break silicon-hydrogen bonds, displacing hydrogen. Given that the displaced hydrogen atom remains near the broken bond, low-temperature annealing is effective in repairing sputter damage.

7. Experimental Section

For conductivity measurements, Corning Eagle glass substrates were utilized. The substrates for FTIR spectroscopy, Raman spectroscopy measurements, and EDX imaging are double-side polished, Phosphorous-doped, <111> oriented silicon wafers. These wafers were 280 µm thick with a resistivity range of 1–5 Ω cm. Lifetime samples are prepared using double-sided textured, quartered M2-sized n-type wafers supplied by LONGi. These wafers were 135 µm thick, have a resistivity of 1 Ω cm, and feature a <100> crystalline orientation.

The cleaning process of the wafers involves a DIO_3 treatment, followed by a dip in HF and a 10 min oxidation in a Piranha solution composed of two parts hydrogen peroxide and one part sulfuric acid. The hydrogenated nanocrystalline silicon carbide layers for all samples were deposited using a Hot-Wire Chemical Vapor Deposition system from MRG Systems. This system includes three curled rhenium filaments of 0.5 mm diameter. The precursor gases for the deposition process consist of 7 sccm monomethylsilane diluted in 70 sccm hydrogen and 25 sccm nitrogen, which serves as a doping source. A double-layer stack structure, beginning with ≈6 nm deposited at a filament temperature of ≈1700 °C, followed by ≈15 nm deposited at a filament temperature of nearly 1990 °C, was prepared. A consistent filament-substrate distance of 71 mm was maintained, with the chamber heater temperature set to 250 °C.

The ITO sputtering process, unless specified otherwise, was carried out from a 97/3 tube target at an 8 cm sample-target distance in a vertical system. The sputter power for this process is 5 kW, with a deposition pressure of 3 µbar and a heater temperature maintained at 250 °C. The rotation speed of the tube target is set to 9 mm s^{-1}, and the gas flow rates for argon and oxygen were 197 and 3 sccm, respectively. If annealing was done, it was performed on a hot plate at 230 °C for 20 min in ambient air.

For conductivity measurements, the ITO was removed by dipping the sample in 37% hydrochloric acid for 18 min. Subsequently, for all conductivity measurements, two coplanar silver pads are evaporated onto the sample, and the conductivity was measured using a custom-built setup. The FTIR spectrometer employed is a Thermofischer Nicolet 5700 FT-IR transmission spectrometer, while the Raman spectrometer is a Renishaw inVia model equipped with a 525 nm excitation laser.

The quasi-steady-state photoconductance measurement to determine the effective minority carrier lifetime and the iV_{OC} was conducted with a Sinton WTC-120 lifetime tester. The iV_{OC} is evaluated under one sun condition, and the τ_{eff} at a charge carrier density of 1×10^{15} cm^{-3}. Photoluminescence images were captured using a Xenics Cheetah 640-CL InGaAs camera cooled to 0 °C. Four images taken during a single illumination cycle allow for the calculation of the photoluminescence lifetime image according to literature.[33] The photoluminescence image is then corrected to the photoconductance lifetime as measured with the Sinton WTC-120 lifetime tester.

Simulations for the electron impact utilize the freeware Monte Carlo Simulation Of Electron Trajectory In Solids (CASINO),[34] while ion impact simulations employ The Stopping and Range of Ions in Matter (SRIM)[35] software. These simulations assume a stoichiometric SiC with an atomic hydrogen concentration of 13 at% and a crystalline volume fraction of 80%, unless otherwise noted. Changes in crystalline volume fraction are simulated by varying the density linearly from 2.4 g cm^{-3} for the amorphous case[36] to 3.21 g cm^{-3} for the crystalline case.[37] The incident energy of electrons and ions is approximated at 270 eV, aligning with the target voltage in the sputtering system.

For electron microscopic analysis of the ITO on nc-SiC:H(n) layers, a cross-sectional TEM lamella is prepared using Ga-focused ion beam (FIB) cutting on a HeliosNanoLab400S FIB. The process (lift-out method) is a multi-step process, including depositing a protective carbon layer, slicing perpendicular to the surface, lifting out the slice with a micromanipulator, mounting it on a Cu TEM support grid, and then polishing it to the desired dimensions and thicknesses. The specimen is cleaned using a UV-based Hitachi HT ZONETEM II cleaner and examined through high-resolution scanning transmission electron microscopy (HR-STEM) on a Hitachi HF5000, operating at 200 kV and equipped with a spherical-aberration (Cs) probe corrector. EDX analyses were conducted using double EDX Ultra 100 detectors from Oxford Instruments.

Supporting Information

Supporting Information is available from the Wiley Online Library or from the author.

© 2024 The Author(s). Advanced Physics Research published by Wiley-VCH GmbH

27511200, 2024, 9, Downloaded from https://onlinelibrary.wiley.com/doi/10.1002/apxr.202400036, Wiley Online Library on [11/09/2024]. See the Terms and Conditions (https://onlinelibrary.wiley.com/terms-and-conditions) on Wiley Online Library for rules of use; OA articles are governed by the applicable Creative Commons License

Acknowledgements

A.E. gratefully thanks Hildegard Siekmann for the sputter depositions and Dr. Elmar Neumann from the Helmhotz Nano Facility[38] at Forschungszentrum Jülich for his support with the scanning electron microscope. Lidia Kibkalo is acknowledged for FIB sample preparation. M.H. and A.M. acknowledge financial support by the Deutsche Forschungsgemeinschaft (DFG) in the project 441718867. The authors acknowledge the support of Hitachi High-Technology.

Conflict of Interest

The authors declare no conflict of interest.

Data Availability Statement

The data that support the findings of this study are available from the corresponding author upon reasonable request.

Keywords

amorphous silicons, silicon carbides, silicon heterojunctions, sputter damage, transparent passivating contacts

Received: March 4, 2024
Revised: May 17, 2024
Published online: July 4, 2024

[1] M. Filipič, Z. C. Holman, F. Smole, S. De Wolf, C. Ballif, M. Topič, *J. Appl. Phys.* **2013**, *114*, 074504.
[2] M. Köhler, M. Pomaska, P. Procel, R. Santbergen, A. O. Zamchiy, B. Macco, A. Lambertz, W. Duan, P. Cao, B. Klingebiel, S. Li, A. Eberst, M. Luysberg, K. Qiu, O. Isabella, F. Finger, T. Kirchartz, U. Rau, K. Ding, *Nat. Energy* **2021**, *6*, 529.
[3] D. Qiu, W. Duan, A. Lambertz, A. Eberst, K. Bittkau, U. Rau, K. Ding, *Sol. RRL* **2022**, *6*, 2200651.
[4] B. Demaurex, S. De Wolf, A. Descoeudres, Z. Charles Holman, C. Ballif, *Appl. Phys. Lett.* **2012**, *101*, 171604.
[5] A. Illiberi, P. Kudlacek, A. H. M. Smets, M. Creatore, M. C. M. van de Sanden, *Appl. Phys. Lett.* **2011**, *98*, 242115.
[6] L. Tutsch, *Implementing sputter-deposited transparent conductive metal oxides into passivating contacts for silicon solar cells, Dissertation*, Universitätsbibliothek Freiburg, Freiburg im Breisgau, Germany **2020**, https://doi.org/10.6094/UNIFR/174516.
[7] Y. Kuang, B. Macco, B. Karasulu, C. K. Ande, P. C. P. Bronsveld, M. A. Verheijen, Y. Wu, W. M. M. Kessels, R. E. I. Schropp, *Sol. Energy Mater. Sol. Cells* **2017**, *163*, 43.
[8] R. Walsh, *Acc. Chem. Res.* **1981**, *14*, 246.
[9] C. G. Van de Walle, R. Street, *MRS Online Proc. Libr.* **1995**, *377*, 389.
[10] C. G. Van De Walle, *Phys. Rev. B* **1994**, *49*, 4579.
[11] R. B. Wehrspohn, S. C. Deane, I. D. French, I. Gale, J. Hewett, M. J. Powell, J. Robertson, *J. Appl. Phys.* **2000**, *87*, 144.
[12] A. Plagemann, K. Ellmer, K. Wiesemann, *J. Vac. Sci. Technol., A* **2007**, *25*, 1341.
[13] T. Welzel, K. Ellmer, *J. Phys. D: Appl. Phys.* **2013**, *46*, 315202.
[14] S. Al Smairat, J. Graham, *J. Appl. Phys.* **2021**, *130*, 125902.
[15] W. Duan, G. Mains, H. T. Gebrewold, K. Bittkau, A. Lambertz, B. Xu, V. Lauterbach, A. Eberst, N. Nicholson, L. Korte, *Adv. Funct. Mater.* **2024**, *34*, 2310552.
[16] W. Beyer, H. Wagner, *J. Appl. Phys.* **1982**, *53*, 8745.
[17] W. Favre, J. Coignus, N. Nguyen, R. Lachaume, R. Cabal, D. Muñoz, *Appl. Phys. Lett.* **2013**, *102*, 181118.
[18] M. B. Pomaska, *Microcrystalline silicon carbide for silicon heterojunction solar cells*, Forschungszentrum Jülich GmbH Zentralbibliothek, Jülich, Germany **2017**.
[19] F. Köhler, T. Chen, M. Nuys, A. Heidt, M. Luysberg, F. Finger, R. Carius, *J. Non-Cryst. Solids* **2012**, *358*, 2012.
[20] J. A. Bearden, *Rev. Mod. Phys.* **1967**, *39*, 78.
[21] R. Rurali, E. Hernández, P. Godignon, J. Rebollo, P. Ordejón, *Comput. Mater. Sci.* **2003**, *27*, 36.
[22] G. Roma, F. Bruneval, L. A. Ting, O. N. Bedoya Martínez, J. P. Crocombette, *Defect Diffus. Forum.* **2012**, *323*, 11.
[23] M. Bockstedte, A. Mattausch, O. Pankratov, *Phys. Rev. B* **2003**, *68*, 205201.
[24] H. Itoh, A. Kawasuso, T. Ohshima, M. Yoshikawa, I. Nashiyama, S. Tanigawa, S. Misawa, H. Okumura, S. Yoshida, *phys. status solidi(a)* **1997**, *162*, 173.
[25] E. Rauls, T. Frauenheim, A. Gali, P. Deák, *Phys. Rev. B* **2003**, *68*, 155208.
[26] M. Rühl, C. Ott, S. Götzinger, M. Krieger, H. B. Weber, *Appl. Phys. Lett.* **2018**, *113*, 122102.
[27] B. Faughnan, A. Moore, R. Crandall, *Appl. Phys. Lett.* **1984**, *44*, 613.
[28] L. Yang, A. Catalano, R. R. Arya, I. Balberg, *Appl. Phys. Lett.* **1990**, *57*, 908.
[29] D. T. Morelli, J. P. Heremans, C. P. Beetz, W. S. Yoo, H. Matsunami, *Appl. Phys. Lett.* **1993**, *63*, 3143.
[30] K. Watari, H. Nakano, K. Sato, K. Urabe, K. Ishizaki, S. Cao, K. Mori, *J. Am. Ceram. Soc.* **2003**, *86*, 1812.
[31] K. T. Regner, D. P. Sellan, Z. Su, C. H. Amon, A. J. McGaughey, J. A. Malen, *Nat. Commun.* **2013**, *4*, 1640.
[32] T. Zhan, Y. Xu, M. Goto, Y. Tanaka, R. Kato, M. Sasaki, Y. Kagawa, *Appl. Phys. Lett.* **2014**, *104*, 071911.
[33] S. Herlufsen, K. Ramspeck, D. Hinken, A. Schmidt, J. Müller, K. Bothe, J. Schmidt, R. Brendel, *phys. status solidi RRL* **2011**, *5*, 25.
[34] H. Demers, N. Poirier-Demers, A. R. Couture, D. Joly, M. Guilmain, N. De Jonge, D. Drouin, *Scanning* **2011**, *33*, 135.
[35] J. F. Ziegler, M. D. Ziegler, J. P. Biersack, *Nucl. Instrum. Methods Phys. Res., Sect. B.* **2010**, *268*, 1818.
[36] L. L. Snead, S. J. Zinkle, *Nucl. Instrum. Methods Phys. Res., Sect. B* **2002**, *191*, 497.
[37] G. L. Harris, *Properties of silicon carbide*, Institution of Engineering and Technology, Stevenage, United Kingsdoms **1995**.
[38] F. Jülich, *J. Large Scale Res. Facil.* **2017**, *3*, A112.

© 2024 The Author(s). Advanced Physics Research published by Wiley-VCH GmbH

27511200, 2024, 9, Downloaded from https://onlinelibrary.wiley.com/doi/10.1002/apxr.202400036, Wiley Online Library on [11/09/2024]. See the Terms and Conditions (https://onlinelibrary.wiley.com/terms-and-conditions) on Wiley Online Library for rules of use; OA articles are governed by the applicable Creative Commons License